Journal of Structural Geology 197 (2025) 105427

Contents lists available at ScienceDirect

Journal of Structural Geology

journal homepage: www.elsevier.com/locate/sg

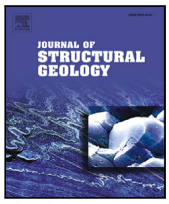

Failure mode transition in brittle boudinage: Effects of cohesion, confining pressure, and layer thickness

Steffen Abe [a], Christoph von Hagke [b,*], Simon Virgo [c], Janos L. Urai [d]

[a] Institute for Geothermal Resource Management, Berlinstr. 107a, Bingen, 55411, Germany
[b] Department of Environment and Biodiversity, Geology Division, University of Salzburg, Hellbrunnerstr. 34, Salzburg, 5020, Austria
[c] Terranigma Solutions GmbH, Laurentiusstraße 59, Aachen, 52072, Germany
[d] Lehr-und Forschungsgebiet für Geologie – Endogene Dynamik (GED), RWTH Aachen University, Lochnerstr. 4-20, Aachen, 52064, Germany

ARTICLE INFO

Keywords:
Boudinage
Failure modes
Numerical modeling
Discrete element

ABSTRACT

Boudins are ubiquitous periodic structures that form during layer-parallel extension of competent material embedded in less competent material. They can have a wide range of geometries, depending on paleo-rheological conditions. This makes them a powerful tool in interpreting the time–temperature and deformation history of a rock package. Consequently, multiple field and modeling studies have described their geometries as well as explored the boundary conditions for their formation. Inspired by previous findings in modeling and field studies, we test the hypothesis that boudin end member geometries, such as pinch-and-swell, domino, torn, and shear band boudins, can be realized with purely brittle–elastic behavior of the boudinaged layer embedded in a viscous matrix. For this purpose, we designed a parametric Discrete Element Modeling study in which different failure modes in the brittle material are achieved by varying the layer thickness, material cohesion and the layer parallel confining stress. We show that the different boudin geometry is a first order result of the failure mode, fracture mechanics in the brittle layer and the associated post failure behavior. Our models confirm previous findings that block rotation of boudins may be associated with coaxial deformation. Our models indicate a failure mode transition exits between torn and drawn boudins. These results may help us better understand the evolution of boudins and thus help interpret natural examples such as the boudin trains in Naxos, Greece.

1. Introduction

Boudins are ubiquitous periodic structures that form when a layer of more competent material, embedded in a matrix of less competent material, deforms during layer-parallel extension (Ramberg, 1955; Ramsay and Huber, 1987; Fossen, 2010; van Noten and Sintubin, 2010). They form in compressional as well as in extensional regimes, typically under direct tension, in shear zones or in limbs of isoclinal folds (Marques et al., 2012; Zulauf et al., 2010; Schöpfer et al., 2009). Boudins exist in a wide range of sizes from μm- to m-scale (Goscombe et al., 2004) to the km-to-crustal scale (Schönherr et al., 2008; Reuning et al., 2009; van Gent et al., 2011; Gueguen et al., 1997; Jolivet et al., 2004). They also occur in many different lithologies, for example in pegmatites forming competent layers in a marble matrix (Schenk et al., 2007), carbonates enclosed in salt (Schönherr et al., 2008), quartz veins in various host rocks (Goscombe and Passchier, 2003), amphibolites in a marble matrix (Bamberg et al., 2022; Virgo et al., 2018; von Hagke et al., 2018), calcite veins in limestone (Grobe et al., 2018), competent units in shale detachments (Morley et al., 2017, 2018), competent sandstones in less competent units (Marques et al., 2012), and many other lithologies (Goscombe et al., 2004). This variability shows that they form over a wide range of pressure and temperature conditions, including brittle as well as ductile deformation. This variability is reflected in the range of the boudin geometries, which are indicative of the properties of the material at the time of deformation, in particular the contrast in viscosity between the competent and the less competent layers (Goscombe et al., 2004; Fossen, 2010; Virgo et al., 2018). The sizes of the boudin blocks are controlled by layer thickness, viscosity contrast and the properties of the interface between the different layers (Bai and Pollard, 1999; Mandl, 2005; Li and Yang, 2007; Iyer and Podladchikov, 2009; Schöpfer et al., 2011). The importance of boudinage was recognized more than a century ago (Lohest, 1909), and since then boudins have been the focus of multiple studies (Quirke, 1923; Corin, 1932; Cloos, 1947). The evolution of boudins has been studied using a wide range of analog (Mandal and Khan, 1991; Zulauf et al., 2009, 2010; Marques et al., 2012) and numerical (Lloyd and Ferguson, 1981; Passchier and

* Corresponding author.
E-mail address: christoph.vonhagke@plus.ac.at (C. von Hagke).

https://doi.org/10.1016/j.jsg.2025.105427
Received 29 June 2024; Received in revised form 25 March 2025; Accepted 2 April 2025
Available online 29 April 2025

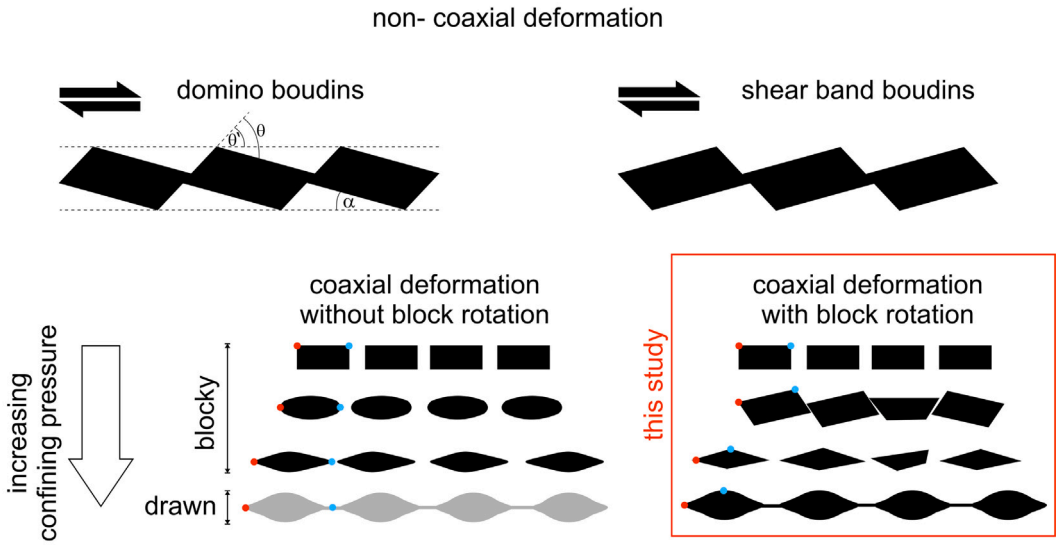

Fig. 1. Classification of boudinage based on geometry. Different types of boudins can form depending on coaxial or non-coaxial deformation as well as confining pressure. Block rotations have commonly been associated with non-coaxial deformation (Goscombe et al., 2004). Coaxial deformation results in blocky boudins with different block shapes, which may however also rotate. By definition based on the curvatures of the boudin exterior surface and face, no transition between torn and drawn boudins is possible. However, in nature such a transition may exist. In this study, we focus on the transition between boudinage types with a particular focus on uniaxial deformation.

Druguet, 2002; Maeder et al., 2009; Schöpfer et al., 2011; Abe and Urai, 2012; Peters et al., 2015; Grasemann et al., 2019) modeling approaches. These studies show that the basic mechanisms of boudin formation are reasonably well understood and that they can be used to explain the influence of layer geometry, rheology, and deformation conditions on the resulting shape and spacing of the boudin blocks. Boudins can be classified based on their geometries (Goscombe et al., 2004) as shown in Fig. 1. Generally, symmetric boudins, which form during coaxial deformation, and asymmetric boudins, which form during non-coaxial deformation, can be distinguished. Typically, asymmetric boudins show rotation of the boudin blocks, and this rotation with respect to the shear plane can be used for boudin classification. However, block rotations can occur also during coaxial deformation, and consequently it may be challenging to distinguish between different boudinage types based on geometry alone (Abe and Urai, 2012; Grasemann et al., 2019). This is particularly relevant as the rock record only rarely allows for direct observation of the time evolution of boudinage structures. Consequently, one aspect that is not well understood is which parameters control the failure mode between boudin blocks and therefore the shape of the block ends.

Understanding block geometry is important, as it may provide insights on material properties during deformation. In this study, we use numerical models to investigate the influence of layer thickness, material strength and stress boundary conditions on the failure modes and resulting shapes of brittle boudins in high spatial resolution.

2. Method

2.1. DEM

The numerical simulations used in this work are based on the Discrete Element Method (DEM). In this approach, which was originally developed by Cundall and Strack (1979) the material is modeled as a collection of particles, which interact with their neighbors and move according to Newton's laws. The key advantage of this method compared to numerical continuum mechanics approaches, like Finite Difference (FD) or Finite Element Method (FEM) approaches, is that the DEM naturally includes the formation and evolution of discontinuities such as brittle fractures into the model. Possible interactions between particles include elastic (Cundall and Strack, 1979; Donzé et al., 1994) and frictional (Place and Mora, 1999) interactions, brittle–elastic bonds (Mora and Place, 1994; Potyondy and Cundall, 2004; Wang et al., 2006) and "dash-pot" interactions (Abe and Urai, 2012). If particles are connected by brittle–elastic bonds, the interaction can break, i.e., be replaced by a combination of a purely repulsive elastic interaction and a frictional interaction. To determine if a bond breaks, the relative displacements of the particles and/or the resulting interaction forces are compared with a given failure criterion. To obtain a realistic fracture behavior, the bonded interaction formulation developed by Wang et al. (2006) is used. This takes into account both translational (i.e., normal and tangential) and angular (bending and torsion) deformation of the bond. The dash-pot interaction developed by Abe and Urai (2012) is used to obtain a ductile material behavior similar to a Bingham material (Middleton and Wilcock, 1994). This implies that, despite the fact that the model consists of individual particles, it is possible to model distributed deformation (as opposed to granular flow only). This is because ductile deformation is scale dependent, and continuous deformation can be localized on the grain scale (Passchier and Trouw, 1996). Consequently, we model deformation that takes place on the grain scale as also observed in natural examples, which we will address in the discussion. Due to the necessary model resolution and consequently the large number of particles contained in the models, the computational cost is relatively high. We have therefore used the parallel DEM software ESyS-Particle (Abe et al., 2003; Weatherley et al., 2010), https://launchpad.net/esys-particle/, to distribute the computational effort across multiple computing nodes on a cluster.

2.2. Stress calculations

Calculating average stresses for a given volume is slightly more difficult in a DEM model compared to a model using a typical continuum-based approach, such as Finite Element or Finite Difference methods. This is in part due to the particle-scale heterogeneity of stresses in DEM models. An additional problem is that the stress tensors can be locally non-symmetric due to rotational degrees of freedom of the particles and angular moments transferred by the interactions.

Three different approaches to calculate the average stress in a volume of a granular medium are described by Fortin et al. (2003): (1) summation of the tensor product of forces and contact orientation vector over all particle interactions within the volume, (2) summation over all external contacts to the volume, and (3) based on the virtual

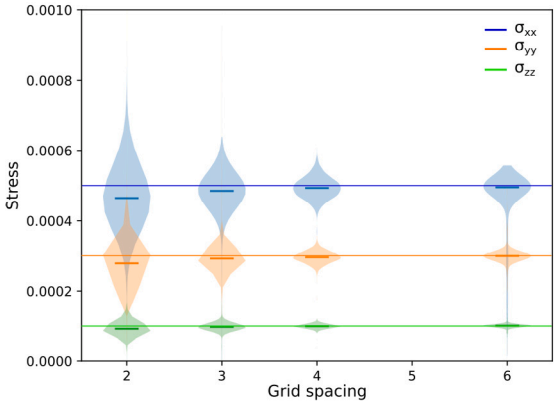

Fig. 2. Distribution of calculated stresses in a triaxial compression model for different cell sizes of the calculation grid. Continuous lines show externally applied stresses, shaded areas show the distribution of calculated stresses in the grid cells and short colored bars show the median values of the distribution. Blue shows σ_{xx}, orange shows σ_{yy} and green shows σ_{zz}.

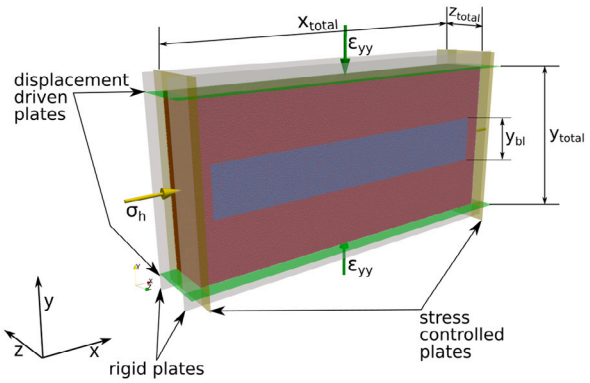

Fig. 3. Model setup. Blue particles show the brittle material, red particles show the ductile material. Transparent yellow planes show the boundary plates where the confining stress σ_h is applied and transparent green planes show the boundary plates which are moved to drive the deformation. The fixed side plates are shown in transparent gray.

work principle. Of these approaches, we chose the second option and use a formulation directly based on the definition of the Cauchy stress to calculate the average stress $\bar{\sigma_{ij}}$ in a given volume V by summing the product of force f and location vector x of all particle–particle interactions where one of the particles involved is inside the volume and the other one is outside, i.e.,

$$\bar{\sigma_{ij}} = \frac{1}{V} \sum_{e} x_i^e f_j^e \tag{1}$$

similar to Eq. 54 in Bardet and Vardoulakis (2001).

The stress calculation algorithm has been validated and the relation between stress grid resolution and the scatter of the calculated stresses has been estimated using data from a true triaxial compression experiment, i.e., $\sigma_{xx} \neq \sigma_{yy} \neq \sigma_{zz}$. In this experiment, a stress of $\sigma_{xx} = 0.0005$, $\sigma_{yy} = 0.0003$, $\sigma_{zz} = 0.0001$ model units is applied to a block of particles with a size of $40 \times 80 \times 40$ model units. Using particle radii in the range $r_{min} = 0.2 \ldots r_{max} = 1.0$ model units, the block contains approximately 365,000 particles. The strength of the bonds between the particles is chosen such that no fracturing is taking place during the loading process. To avoid boundary effects that influence the observed stress distributions, the stress was calculated for a volume of size $36 \times 72 \times 36$ inside the model, i.e., leaving a distance of at least two model units (i.e., twice the maximum particle radius) between the calculation volume and the boundary of the model.

The results (Fig. 2) show that the calculated stresses converge towards the expected values with increasing cell size of the calculation grid. For the particle packing used in the validation model, which is the same as in the models shown in the following sections, a grid cell size of three model units, i.e., three times the maximum particle radius, appears to provide the best compromise between grid resolution and the accuracy of the calculated stresses.

2.3. Model setup

Although the models are deformed under plane strain conditions, we chose to use 3D models instead of a computationally cheaper 2D approach. The main reason for this decision is that granular shear zones, such as those developing between boudin blocks in some of the models, show differences in their mechanical properties, in particular in their macroscopic friction angles, in 2D and in 3D (Frye and Marone, 2002; Hazzard and Mair, 2003). We use a three-layer model where a competent brittle–elastic layer is sandwiched between two less competent ductile layers (Fig. 3). The layers are arranged parallel to the x–z plane. The model is using a central layer with a finite length, i.e., the brittle–elastic layer is shorter than the complete model. The space between the layer terminations and the boundary plates is filled with ductile material. 2D studies using a similar setup have shown that the details of the end of the layer do not significantly influence the evolution of the fracture in the competent layer (Abe and Urai, 2012). However, the fact that the ends of brittle layer are not in direct contact with the boundary plates does avoid a possible boundary effect on the rotation of the boudin blocks closest to the boundary. Rigid plates on the outer surfaces of the model are used to control deformation of the particle assembly. The xy-boundaries are fixed, preventing deformation of the model in z-direction and resulting in a plane strain deformation regime. The yz-boundaries on the +x- and -x-ends of the model are servo-controlled to stay at a given confining stress, which is held constant after an initial ramp-up phase. xz-boundaries (i.e., top- and bottom) are initially loaded at the same stress as the boundaries at the +x and -x ends of the model until the desired confining stress is reached. After this, they are moved towards each other to shorten the model in the y-direction, i.e., perpendicular to layering. The rate of movement is also kept constant after an initial ramp-up phase. To avoid discontinuities in the velocity of the plate movement, and therefore spikes in the forces applied to the particles adjacent to the plates, a sinusoidal function has been used to ensure a smooth transition between the applied stress- or velocity values before and after ramp-up

$$f(t) = f_0 + (f_1 - f_0) \sin\left(\frac{\pi}{2} \frac{t - t_0}{t_1 - t_0}\right) \tag{2}$$

where f_0 is the applied value before the ramp-up and f_1 is the value afterwards, t_0 the time step when the ramp begins, t_1 when it ends and t is the current time step. The simulation ends when 25% vertical shortening is achieved. Having checked that the kinetic energy of the particles in the model remains much smaller than the elastic energy stored in the bonds ensures that the deformation rates are slow enough so that the simulations can be considered quasistatic, similar to previous work on 2D-boudinage models (Abe and Urai, 2012).

In the brittle–elastic material, particles are initially interacting by breakable bonded interactions and by frictional-elastic interactions after the bonds are broken. In the ductile material, particles are not bond together and do not mutually interact (cf (Abe and Urai, 2012)). A range of different model geometries were used in the simulations. For the main part of the work, two sets of simulations were performed based on model geometries "Thin" and "Thick" (Table 1) with the same length x_{total} and width z, but different layer thicknesses. In total, we present 56 simulations. Four different values of bond cohesion, C_{bond}, for the brittle layer, 50 MPa, 75 MPa, 100 MPa and 150 MPa,

Table 1
Geometric parameters of main model sets. All parameters in model units. For the meaning of the parameters see also Fig. 3.

	"Thin"	"Thick"	"Long1"	"Long2"
length (x_{total})	220	220	330	440
brittle layer length (x_{bl})	200	200	310	420
width (z_{total})	30	30	30	30
thickness (y_{total})	50	100	100	100
brittle layer thickness (y_{bl})	10	30	30	30
min. particle radius	0.2	0.2	0.2	0.2
max. particle radius	1.0	1.0	1.0	1.0

were used, resulting in the properties of the material as listed in Table 2. This was combined with seven different confining stresses between 1 MPa and 100 MPa for a total of 28 simulations for each model geometry.

In previous numerical models, it has been shown that the detailed shape of the layer terminations does not affect the outcome of the deformation process (Abe and Urai, 2012). In other words, whether the brittle layer is as long as the whole model, i.e., in direct contact with the boundary plates in the longitudinal (x) direction, or slightly shorter, does not change the model results. We use a geometry with a slightly shorter brittle layer. The gap between the ends of the brittle layer and the edge of the model was 10 model units in all models, i.e., the length of the brittle layer x_{bl} is constant at 20 units smaller than the total length of the model. A summary of the geometric parameters of all models used is provided in Table 1. The geometric properties of the models are given in dimensionless model units because the processes and structures modeled are not tied to a particular scale but occur in a variety of sizes in nature. A scaling to some defined size, e.g., for comparison with a specific natural example, can easily be achieved by assigning a defined real-world length to the model length unit. The models remain valid independent of the chosen length scale, as dynamic similarity (Hubbard, 1937) is ensured by defining the model boundary conditions in terms of stresses and not forces, and a kinematic similarity criterion does not apply due to the quasi-static nature of the deformation.

Both model materials are composed of particles with a radius ranging between $r_{min} = 0.2$ and $r_{max} = 1.0$ model units. The particles are packed in the respective volumes using the insertion-based algorithm of Place and Mora (2001), resulting in a dense, stress-free initial arrangement of the particles. Using these parameters, the model geometries contain a relatively large number of particles: $n_p \approx 900$ k for the "Thin" models and $n_p \approx 1.7$ M for the "Thick" models. Additional, longer models used to test that the deformation characteristics of the brittle layer are not determined by finite length effects of the model, using lengths of $x_{total} = 330$ and $x_{total} = 440$, result in $n_p \approx 2.6$ M and $n_p \approx 3.4$ M particles respectively.

The material parameters for the ductile material are kept constant for all models, using a particle scale viscosity constant $A = 0.01$ for the dashpot interactions (Abe and Urai, 2012) and a Young's Modulus $E = 10$ GPa for the elastic interactions. In the brittle layer, a brittle beam model (Weatherley, 2011) is used to parameterize the bonded interactions, and a Young's Modulus of $E = 30$ GPa and a Poisson's ratio of $\nu = 0.3$ are used for the elastic parameters. The bond cohesion C, which, together with the angle of internal friction ϕ, determines the failure strength of the bonds, is varied between $C = 50$ MPa and $C = 150$ MPa for the different simulations. The coefficient of internal friction used in the failure criterion of the bonded interactions is kept constant for all models at $\tan\phi = 0.6$, i.e., $\phi = 30.96\,\mathrm{deg}$. If bonds are broken in the brittle material, the particles will interact by elastic-frictional interactions using the same Young's Modulus of $E = 30$ GPa, and a coefficient of friction of $\mu = 0.6$ in cases where they come into contact again. The interaction between the brittle and the ductile materials along the interface between the layers is also implemented using frictional interaction with $\mu = 0.6$.

Table 2
Macroscopic strength parameters of the model material for different values of the bond cohesion C_{bond}: Cohesion C, tensile strength T, unconfined compressive strength UCS and angle of internal friction φ.

C_{bond} [MPa]	50	75	100	150
C [MPa]	46.1 ± 0.7	66.3 ± 0.7	89.3 ± 1.0	117.8 ± 2.4
T [MPa]	41.6 ± 2.3	60.3 ± 2.3	76.2 ± 3.7	116 ± 5
UCS [MPa]	147 ± 3	215 ± 3	285 ± 5	422 ± 8
φ [deg]	23.4 ± 0.7	24.8 ± 0.3	25.0 ± 0.5	29.6 ± 0.7

2.3.1. Calibration of brittle material

The strength parameters of the brittle model material were calibrated using a range of simulated triaxial tests. A defined confining stress was applied to the front and back sides, i.e., those normal to the x-axis, of block shaped samples with x:y:z aspect ratio 1:2:1, and containing ≈ 45000 particles. The samples where then loaded to failure by applying an increasing compressive or tensile strain to the top and bottom sides of the sample. During the deformation process, the strain rate is held constant after an initial ramp-up phase.

The set of simulations is designed to generate 2D failure envelopes, i.e., only considering the $\sigma_1 - \sigma_3$-plane and not explicitly varying σ_2. To obtain failure envelopes most appropriate to the stress and strain conditions in the boudinage experiments, the triaxial tests have been performed in plane-strain conditions, i.e., $\epsilon_z = 0$ is enforced using rigid side walls on the sample similar to the fixed side plates in the boudinage models. From the σ_1 and σ_3 values at sample failure obtained for a range of confining stresses, a failure envelope in the $\sigma - \tau$ (Mohr) - space is derived by computing the common tangents of neighboring Mohr-circles (Pincus, 2000) and combining the resulting points on the circles. Data from a set of tests on five samples are combined to estimate the uncertainty of the failure parameters resulting from the variability in particle packing between samples. The result is a failure envelope, which can be reasonably well approximated by a linear Mohr–Coulomb law in the compressive field. In the tensile field, the failure envelope can be approximated by a parabolic shape, i.e., $\tau^2 = p(\sigma - T)$, where T is the unconfined tensile strength of the material. Correlation coefficients are $r > 0.99$ in all cases.

The tests are performed with the four different values of the bond cohesion C_{bond}, which were also used in the boudinage models in the main part of the work, i.e., 50 MPa, 75 MPa, 100 MPa, and 150 MPa. Comparing the failure envelopes obtained for the different values of C_{bond} (Fig. 4a), it can be seen that the macroscopic strength parameters of the model material (Table 2), i.e., cohesion, unconfined compressive and tensile strengths, show a linear dependence on C_{bond} (Fig. 4b), whereas the angle of internal friction remains nearly constant. The results also show a ratio between unconfined compressive and tensile strength of UCS/T ≈ 3.5. This is lower than most natural rocks where values of UCS/T > 10 are common (Jaeger et al., 2007; Fjaer et al., 2008) but not unusual for fully bonded materials in DEM models (Abe and Urai, 2012; Schöpfer et al., 2009).

3. Results

Structures formed in a thin brittle layer, i.e., $y_{bl} = 10$, show a transition between blocky torn boudins at low confinement, σ_{xx}, and high strength of the brittle layer, C_{bond}, to drawn boudins in the high confinement/low strength field (Fig. 5). The models with high confinement and low strength ($C_{bond} = 50$ MPa, $\sigma_{xx} = 50$ MPa or 100 MPa and $C_{bond} = 75$ MPa, $\sigma_{xx} = 100$ MPa) might geometrically look like pinch-and-swell structures, but kinematically they are still drawn boudins, i.e., no thickening is taking place.

Models with a thick brittle layer, i.e., $y_{bl} = 30$, show blocky torn boudin structures in the low confinement/high strength field of the parameter space, similar to models with a thin brittle layer (Fig. 6). In the high confinement/low strength field, however, the transition is

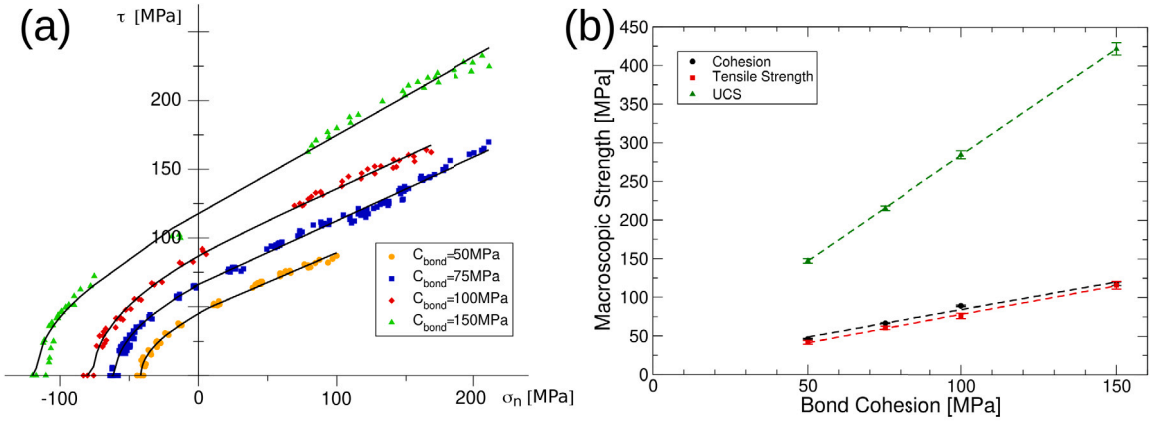

Fig. 4. Results of strength calibration. (a) failure envelopes for different values of the bond cohesion C_{bond}. Colored symbols: points on the failure envelope calculated according to Pincus (2000), black lines: calculated using least squares fits to a parabolic function in the tensile field and a linear function in the compressive field. (b) dependence of macroscopic strength parameters on bond cohesion C_{bond}. C: cohesion, T: tensile strength, UCS: unconfined compressive strength. Symbols and error bars: data calculated from failure envelopes in (a), dashed lines: linear least squares fit.

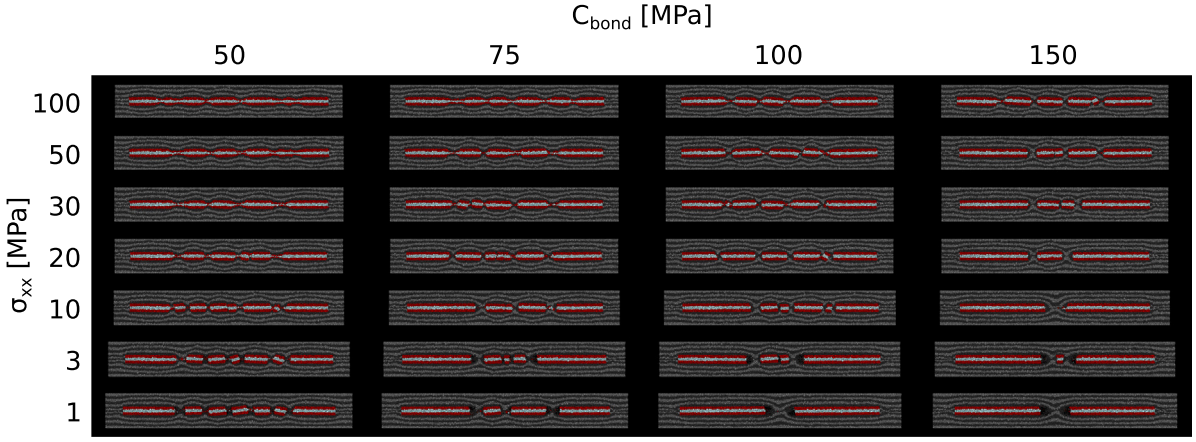

Fig. 5. Deformation patterns for models with thin brittle layer ($y_{bl} = 10$) for different confining stresses σ_{xx} and bond strengths (cohesion C_{bond}). Deformation transitions from blocky torn boudins to drawn boudins. Small boudin blocks partly show clockwise or counterclockwise rotation.

not towards drawn boudins as in the thin models, but shear bands form between the boudins. We note, however, that, as deformation is coaxial, the shearbands have no preferred orientation but form conjugate sets. The models at very high strength (C_{bond} = 150 MPa) and low to intermediate confinement, and those at intermediate to high strength and low confining stress, do not fail at all in the present series of simulations.

In order to test that the difference in the failure mode between the "thin" and the "thick" models is not due to the changed aspect ratio of the brittle layer ($y_{bl} : x_{bl} = 1 : 20$ in the "thin" and $y_{bl} : x_{bl} = 1 : 6.66$ in the "thick" models), additional "thick" models with a larger model length were run. Using total model lengths $x_{total} = 330$ and $x_{total} = 440$ results in an aspect ratio of the brittle layer of $y_{bl} : x_{bl} = 1 : 10.33$, and $y_{bl} : x_{bl} = 1 : 14$ respectively (Models "Long1" and "Long2" in Table 1). Structures resulting from deformation at confining stresses of σ_{xx} = 10 MPa and σ_{xx} = 50 MPa (Fig. 7) using a bond cohesion of C_{bond} = 75 MPa show that the failure modes do not change with layer length.

3.1. Stress and failure modes

The stress inside the central part of the brittle layer, i.e., the part where the main fracture nucleates at a later stage of deformation, was calculated as described in Section 2.2. This is necessary to investigate the relationships between the stress applied to the whole model by external forces using the boundary walls, and the internal stresses within, and the brittle layer. Secondly, it is needed to understand the relationship between the stresses in the brittle layer and characteristics of the subsequent failure. The externally applied stresses are calculated directly from forces on walls and the positions of the walls. Because the boundary walls do not transmit shear forces to the model, the off-diagonal elements of the stress tensor are all zero, i.e., $\sigma_{xy} = \sigma_{xz} = \sigma_{yz} = 0$, and the principal stresses can directly be obtained from the diagonal elements of the stress tensor, σ_{xx}, σ_{yy} and σ_{zz}.

The data shows that the stresses inside the brittle layer are different from the externally applied stresses. In particular, all externally applied stresses are compressive, whereas inside the central part of the brittle layer, the minimum principal stress, σ_3, is negative, i.e., tensile (orange vs. black semicircles in Fig. 8).

In the model with high confinement (σ_{xx} = 50 MPa), which displays shear failure, the internal stress state is compatible with the observed failure mode. While the average stress state in the central part of the brittle layer (black semicircle in Fig. 8 b) has not yet reached the critical stress (green failure envelope in Fig. 8 b), shear failure is triggered. This is because the stress distribution is sufficiently heterogeneous so that some volume within the brittle layer is in a critical stress state. Additionally, the orientation of the shear planes is compatible with the expected values. Based on an angle of internal friction of the model material, $\varphi \approx 25\,\text{deg}$ (Table 2), an angle of around 57.5 deg between the layer-normal direction and the failure plane would be expected.

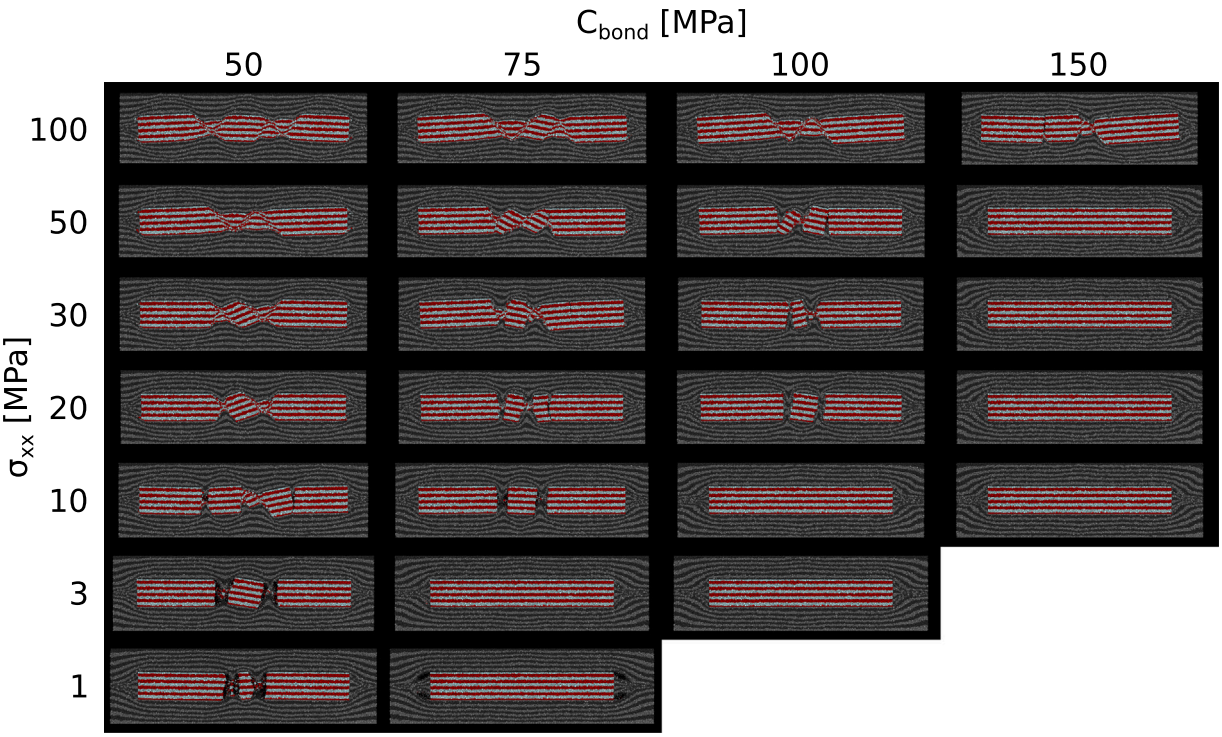

Fig. 6. Deformation patterns for models with thick brittle layer ($y_{bl} = 30$) for different confining stresses σ_{xx} and bond strengths (cohesion C_{bond}). Non-fracturing high strength/low confinement models in the bottom right corner not shown for clarity.

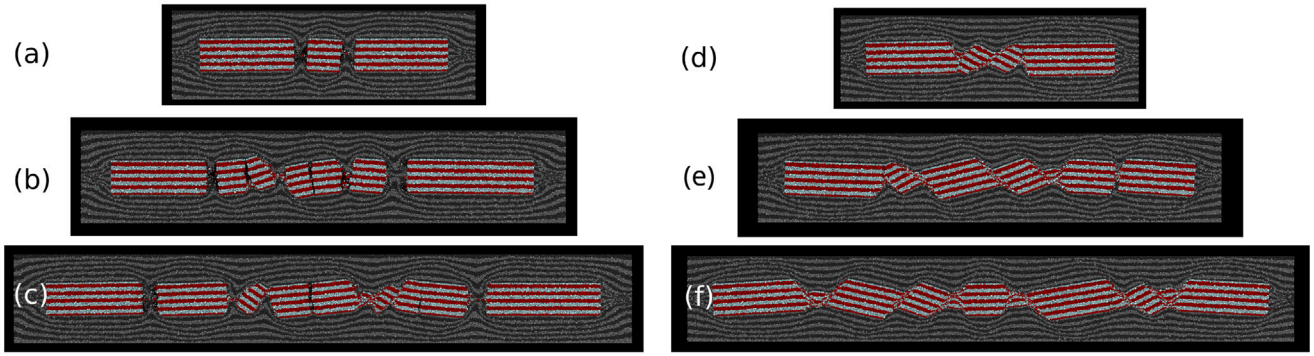

Fig. 7. Boudin structures for different layer lengths at the same brittle layer strength $C_{bond} = 75$ MPa. left column (a, b,c) confinement $\sigma_{xx} = 10$ MPa, right column (d, e, f) confinement $\sigma_{xx} = 50$ MPa. (a), (d) brittle layer length $x_{bl} = 200$, (b), (e) $x_{bl} = 310$, (c), (f) $x_{bl} = 420$.

The observed initial orientations fall in the range of $\varphi = 52 - 56$ deg (Fig. 9).

In models where the brittle layer undergoes tensile failure, the average stress state immediately before failure is further away from the failure envelope as compared to shear failure (Fig. 8 a). Based on the calculated heterogeneity of the stress state, the distance to the failure envelope is about two standard deviations, compared to slightly less than one standard deviation in models with shear failure (compare semi-circle blue areas in Figs. 8). This suggests that a much smaller part of the brittle layer needs to be in (or near) a critical stress state to cause tensile failure. Furthermore, in the case of tensile failure, the observed pre-failure stress state does not match the failure mode as well as that observed in the case of shear failure. The data (Fig. 8 a) show that σ_3 is tensile, but the position of the Mohr circle is more compatible with hybrid shear/tensile failure than with pure tensile failure. Videos showing the evolution of stresses in the brittle layer for two models ($C_{bond} = 100$ MPa, $\sigma_{xx} = 100$ MPa and $C_{bond} = 50$ MPa, $\sigma_{xx} = 3$ MPa) are available in the supplementary material.

4. Discussion

The results of the numerical models show that the change in failure mode with brittle layer thickness under high confinement stress conditions is due to the relationship between the thickness of the brittle layer and the thickness of the shear bands developing at the point of failure. The thickness of the shear bands is approximately 4–5 model units (Fig. 9). The mean particle radius in the model material of ≈ 0.325 model units represents a width of approximately 6–8 particles across the shear band. This is compatible with what is known about typical shear bands in granular materials, which generally are in the range between 6 and 10 particles wide (Roscoe, 1970; Mühlhaus and Vardoulakis, 1987). This also means that the model resolution needs to be high enough to actually resolve the shear bands in order to correctly model the evolving structures, i.e., as a result of the finite shear band thickness, the geometrical constraints prevent the formation of shear bands if the brittle layer thickness is not significantly larger than the typical shear band width of the material. In models with thin geometry (Table 1), the brittle layer is only about twice as thick as the shear band in this

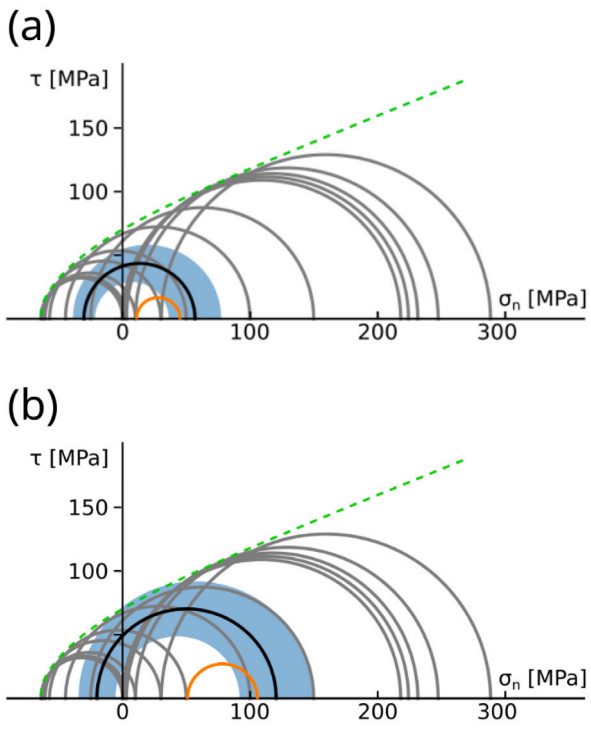

Fig. 8. Stress state in the central part immediately before failure in the model with C_{bond} = 75 MPa, confinement σ_{xx} = 10 MPa (a) and σ_{xx} = 50 MPa (b) vs. failure envelope of the material. Gray semicircles: stress states from triaxial tests used for the calculation of the failure envelope (Section 2.3.1), green dashed line: estimated failure envelope, black semicircle: average stress state in the central part of the brittle layer, blue area: average stress state plus/minus one standard deviation, orange semicircle: externally applied stress.

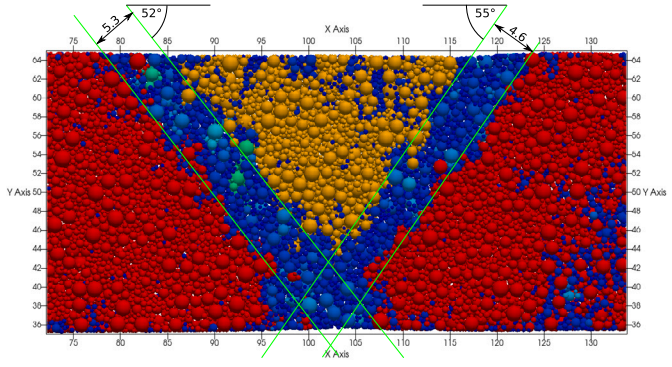

Fig. 9. Detailed view of conjugate shear zones in the model with a thick brittle layer, bond cohesion C_{bond} = 75 MPa and confining stress σ_{xx} = 100 MPa along a slice through the center of the model parallel to the x–y-plane. Particles are colored by size of the block to which they belong (blue/green: small grains, orange/red: large blocks).

material, i.e., 10 model units vs. approximately 5 model units (Fig. 9). This does not allow the shear bands to form. In contrast, the brittle layer in the models with the thick geometry is about 6 times as thick as the shear bands, therefore allowing them to form. In addition, the brittle layer requires a minimum length so that boudins can form because the length of the boudin blocks is determined by layer thickness and boundary conditions.

Some models at intermediate conditions, e.g., the one at C_{bond} = 75 MPa, σ_{xx} = 50 MPa in Fig. 6, could possibly also be considered domino boudins. However, following the nomenclature of Goscombe et al. (2004), asymmetric boudins, such as domino boudins or shear band boudins, are associated with non-coaxial deformation. Our models are coaxial, and thus domino or shear band boudins are not expected. However, it has been shown that block rotations can also occur during coaxial deformation depending on the layer thickness ratio (i.e., thickness ratio of the brittle and ductile layer) and strength ratio (i.e., tensile strength in the brittle layer divided by the flow strength in the ductile layer) (Abe and Urai, 2012; Mandal et al., 2000). These boudins have been termed shear fracture boudins (Mandal et al., 2000). As the terms "shear band boudin" and "shear fracture boudin" can be easily confused, as they both point to the existence of shear fracturing, we propose to use instead the terms symmetric or asymmetric shear band boudin to better match the nomenclature of Goscombe et al. (2004). Symmetric shear band boudins bridge the gap between torn boudins and drawn boudins (Fig. 10).

Calculating the stress state of the brittle layer immediately before failure shows that the failure mode is compatible with the stress state observed in the shear failure case (Fig. 8 b). However, there is a discrepancy in the case of tensile failure (mode-1, Fig. 8 a). The issue that the stress circle is still well away from the failure envelope of the brittle material obtained from triaxial tests (Section 2.3.1) can be explained by stress heterogeneity. However, it remains unclear why the stress circle is farther away from the failure envelope in the tensile case than in the shear case. Given that the heterogeneity of the stress distribution in both cases is similar (see light blue areas in Fig. 8), this also means that in the tensile case, a smaller part of the brittle layer needs to reach a critical stress state to cause failure. Alternatively, the effect might be related to the observation that in DEM simulations the tensile strength of the material tends to show a stronger variability at the same spatial scale as the compressive strength (cf. Fig. 2 h in Schöpfer et al., 2007). In addition, the calculated Mohr circle in the models that fail in tension indicate a hybrid tensile/shear failure rather than shear failure only, because its closest point to the failure envelope is well away from $\tau = 0$. The reason for this discrepancy is unclear. One factor might be the inability of the stress calculation procedure to resolve highly localized stress concentrations prior to macroscopic failure. Another possible cause is the difference in boundary conditions between the triaxial tests used to calculate the failure envelope and the actual boudinage models. However, a detailed investigation of the effect is beyond the scope of this work. Additionally, it may be necessary to consider that the difference in the ratio between the tensile and compressive strengths of the DEM material compared to most rocks is likely to have an influence on the failure modes of the material under certain stress conditions. In particular, the transition from mode 1 (tensile) to hybrid failure is likely to happen at a lower mean stress in the DEM models than would be expected in rocks with the same tensile strength. This should be taken into account when trying to quantitatively compare the failure modes observed in the models to specific stress/strength conditions in real rocks under very low mean stress.

Geometries observed in our models can be compared to natural boudinage. Using the classification of Goscombe et al. (2004), models with thick boudinage plot in the field between gash and domino boudins (Fig. 10). This is because the blocks rotate during deformation. However, in our models, no bulk shear is applied. It has been shown earlier that block rotations can occur without the presence of bulk shear (Abe and Urai, 2012; Passchier and Druguet, 2002; Grasemann et al., 2019). The presence of shear bands between the boudin blocks therefore does not automatically mean that they are actually shear band boudins, as defined in Goscombe et al. (2004). They can also be classified as domino boudins based on their geometry. Theoretically, it is possible to distinguish boudins with bulk shear from torn boudins based on the termination, i.e., the angle between the exterior surface of the boudin and the inter-boudin plane (Θ after (Goscombe et al., 2004)). In the case of torn boudins, the angle is comparably large, as it can be explained by shear fracturing in a Mohr–Coulomb environment. Domino and shear band boudins can rotate much more, leading to Θ angles that can be < 45°. Therefore, ductile deformation can be

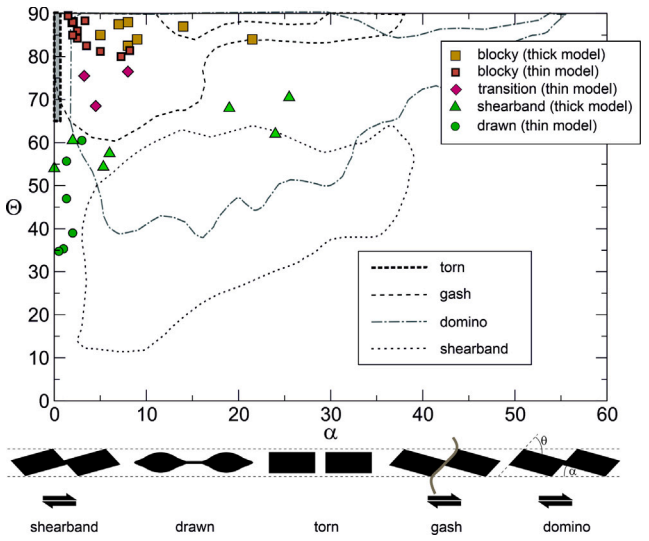

Fig. 10. Boudin block shape vs. block rotation angle. Θ is the angle between boudin exterior and inter-boudin interface as defined in Goscombe et al. (2004), α is the block rotation angle. Dashed and dotted lines show the outlines of the fields for different boudin types adapted from Fig. 7 in Goscombe et al. (2004), symbols show data from this work. A transition between torn, shear band and drawn boudins becomes apparent.

inferred in the field if Θ angles are smaller than 45°. Our findings may help understand the transition between different end-member types of boudinage. While in natural examples commonly one type of boudinage is dominant, transitions between end-members have been described (Goscombe et al., 2004). Our models contribute towards the understanding of the mechanical conditions under which such transitions occur. This study focuses on the fully brittle to brittle–ductile domain, but similar transitions may occur in the ductile regime.

We apply our modeling results to the multiple boudins exposed in Naxos, Greece (Schenk et al., 2007; Bamberg et al., 2022; von Hagke et al., 2018; Virgo et al., 2018). Here, multiple phases of boudinage and folding record the internal deformation of the migmatitic center of the Naxos metamorphic core complex from high-grade metamorphic conditions over the pro- and retrograde path to shallow deformation (Cao et al., 2017; Lamont et al., 2023). This is witnessed in amphibolite and pegmatite layers embedded in marble (Fig. 11). The decrease in temperature and pressure is particularly well recorded in the embrittlement of amphibolite and marble during exhumation and by mineral assemblages associated with the respective structures that change from biotite to chlorite and secondary calcite (Virgo et al., 2018). This led to the formation of five distinguishable generations of boudinage, which are, old to young, long-wavelength pinch and swell boudins, short-wavelength pinch and swell boudins, domino boudins, torn boudins and hairline veins (Virgo et al., 2018; von Hagke et al., 2018). All boudin generations indicate E-W shortening with different orientations of layer parallel extension, rotating in the plane of layering from vertical over south vergent and horizontal to north vergent. Strain progressively decreases from ≫100 percent elongation in the long-wavelength pinch-and swell boudins over about 10 percent in domino boudins to approximately one percent in the hairline veins (Virgo et al., 2018). This offers insights into the evolution of boudins under progressively decreasing strains, pressures and temperatures.

Our models are representative of the brittle phase boudins, i.e., the torn and domino or shear band boudinage. Fig. 11 shows a compilation of structures observed in the field. Many boudin geometries indicate non-coaxial deformation because of a strong predominance of one dip direction of boudin interfaces. However, particularly in boudins that formed at a late stage of deformation (cf. von Hagke et al., 2018), shear fractures dipping in opposite directions can be observed. These geometries are akin to our model observations and can thus be interpreted as symmetric shear band boudins.

As observed in our models, in natural examples shear fracturing cannot be observed macroscopically in layers thinner than approximately 10 mm (Bamberg et al., 2022). Instead, layers fail in a ductile manner. Our models provide an explanation for that behavior. However, based on the observation that the mean spacing of boudins and lateral dimensions is largely independent on the thickness of the amphibolite, it has also been shown that the mechanical unit in part consists not only of the amphibolite, but also includes the surrounding marble (Virgo et al., 2018). In this case, it is expected that fractures will crosscut lithological boundaries. Although this can be observed for the latest stage of deformation in the Naxos boudins (Bamberg et al., 2022; Virgo et al., 2018; von Hagke et al., 2018), it is not the case in the domino boudins.

The amphibolites in Naxos underwent boudinage in five phases under different boundary conditions during exhumation. Therefore, different types of boudinage are present within single boudinage trains (Bamberg et al., 2022; Virgo et al., 2018; von Hagke et al., 2018; Schenk et al., 2007), Fig. 11. Based on our models, it is possible to interpret the different geometries as the result of constant exhumation and thus transition between different types of boudinage (Fig. 12). Early drawn boudins were later overprinted by shear band boudins and torn boudins, witnessing the constant lowering of confining pressure (Fig. 12). Different types of boudinage have been preserved because of a rotation of the regional stress field with respect to the amphibolite layers (Virgo et al., 2018). Using our models as pressure gauges for the natural examples, this would imply that late stage deformation in Naxos occurred at pressures possibly as low as 30 MPa (Fig. 6), which translates to depths of approximately 3 km based on the relatively low strength of the amphibolite.

5. Conclusions

We studied the dependence of failure modes and the resulting structures on the initial layer thickness, material parameters and applied boundary conditions. The results of our models confirm that a range of boudinage behaviors can be achieved in the parameter space of cohesion and confinement, from pinch to swell to torn boudins. A higher confinement and lower cohesion contribute to the change of the failure mode in a qualitatively similar way. We show that:

- Transition from blocky torn boudins to drawn boudins can be modeled as a function of material strength and confining pressure.
- Local heterogeneities can cause shear failure already before critical stress of the entire rock column is reached.
- In the pinch-and-swell regime (high confinement, low cohesion), a high number of bond breaks throughout the brittle layer lead to weakening of the brittle layer before extensional strain. Pinch-and-swell boudins form as the layers progress in extension as the layer deforms along conjugated slip planes and by granular flow of the particles.
- In the transition regime (lower confinements, higher cohesion), bond breakage localizes in wide zones (i.e., as thick as, or thicker than, layer thickness) in small scale conjugated shear and hybrid fractures. This results in necks of highly deformed material between intact blocks of the brittle layer. The boudins have a more angular shape and block rotation is more common than in the flow regime.
- In the torn boudin regime (low confinements and/or high cohesion), the distributed damage in the layer is low and failure occurs in localized mode-I fractures.
- These models can be used to better understand natural examples of boudinage.

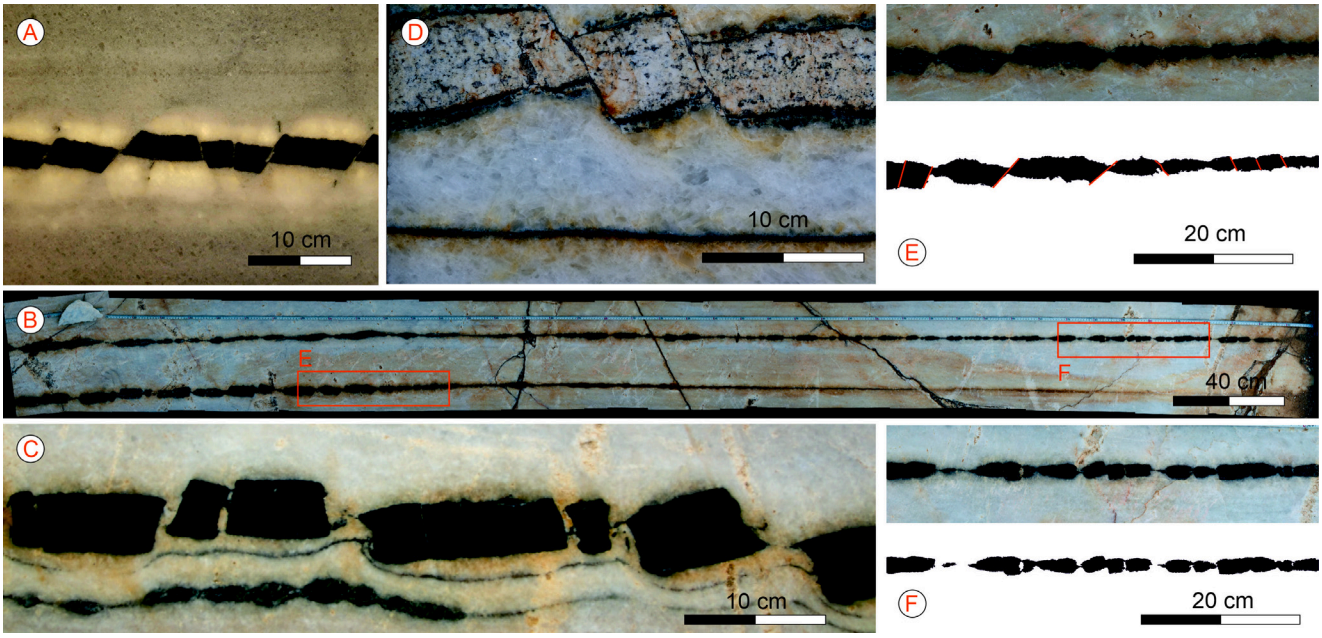

Fig. 11. Examples from boudinage structures from Naxos, Greece. A: boudin train under transmitted light showing blocks bound by shear fractures dipping in opposite directions. These may have formed during coaxial deformation. Note thin vertical chlorite filled veins above and below the amphibolite layer, which are tension gashes. Consequently, some of the boudins classify as gash boudins. B: Several meter log boudin train as exposed in the marble quarries. Details shown in E and F. C: torn boudins with concave faces (modified after (Virgo et al., 2018). D: Boudinaged pegmatite layer. Without the presence of shear fractures dipping in the opposite direction, it is challenging to distinguish between boudins that formed under coaxial or non-coaxial conditions. E: Detail of large boudin train and interpretations. Boudin blocks with shear failure in two conjugate dip directions may indicate late coaxial deformation and a transition between drawn and torn boudins. F: Detail of large boudin train shown in B. Drawn boudins within the same boudin train indicate the transition from ductile to brittle boudinage. See Virgo et al. (2018), von Hagke et al. (2018) for more details on multiple boudinage phases within these layers.

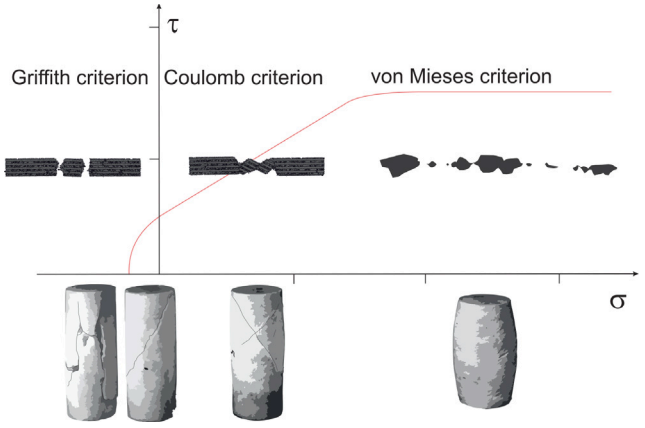

Fig. 12. Concept of transition between torn boudins to shearband boudins and drawn boudins during coaxial deformation. Here, boudin geometries are akin to classic rock mechanical tests, and differences form as a result of different confining pressures. Rock deformation experiments based on Paterson and Wong (2005).

CRediT authorship contribution statement

Steffen Abe: Writing – review & editing, Writing – original draft, Software, Methodology, Investigation, Formal analysis. **Christoph von Hagke:** Writing – review & editing, Writing – original draft, Project administration, Investigation, Funding acquisition, Conceptualization. **Simon Virgo:** Writing – review & editing, Software, Investigation, Formal analysis, Conceptualization. **Janos L. Urai:** Supervision, Investigation, Funding acquisition, Conceptualization.

Declaration of competing interest

The authors declare the following financial interests/personal relationships which may be considered as potential competing interests: Christoph von Hagke reports financial support was provided by German Research Foundation. If there are other authors, they declare that they have no known competing financial interests or personal relationships that could have appeared to influence the work reported in this paper.

Acknowledgments

This work was partly funded by the Deutsche Forschungsgemeinschaft (DFG), Germany as part of the project "BoDy – Boudinage Dynamics" (UR 64/14–1). We thank two anonymous reviewers for constructive comments, and the editors of this special commemorative issue to Janos Urai.

Appendix A. Supplementary data

Supplementary material related to this article can be found online at https://doi.org/10.1016/j.jsg.2025.105427.

Data availability

No data was used for the research described in the article.

References

Abe, S., Place, D., Mora, P., 2003. A parallel implementation of the lattice solid model for the simulation of rock mechanics and earthquake dynamics. Pure Appl. Geophys. 161.

Abe, S., Urai, J.L., 2012. Discrete element modeling of boudinage: Insights on rock rheology, matrix flow and evolution of geometry. J. Geophys. Res. 117 (B01407), http://dx.doi.org/10.1029/2011JB008555.

Bai, T., Pollard, D.D., 1999. Spacing of fractures in a multilayer at fracture saturation. Int. J. Fract. 100, L23–L28.
Bamberg, B., von Hagke, C., Virgo, S., Urai, J.L., 2022. Spacing and strain during multiphase boudinage in 3D. J. Struct. Geol. 161, 104636. http://dx.doi.org/10.1016/j.jsg.2022.104636, URL https://www.sciencedirect.com/science/article/pii/S0191814122001286.
Bardet, J., Vardoulakis, I., 2001. The asymmetry of stress in granular media. Int. J. Solids Struct. 353–367.
Cao, S., Neubauer, F., Bernroider, M., Genser, J., Liu, J., Friedl, G., 2017. Low-grade retrogression of a high-temperature metamorphic core complex: Naxos, Cyclades, Greece. Bulletin 129 (1–2), 93–117.
Cloos, E., 1947. Boudinage. Eos, Trans. Am. Geophys. Union 28 (4), 626–632.
Corin, F., 1932. A propos du boudinage en Ardenne. Bull. Geol. Soc. Belg. 42, 101–117.
Cundall, P.A., Strack, O., 1979. A discrete numerical model for granular assemblies. Géotechnique 29, 47–65.
Donzé, F., Mora, P., Magnier, S.A., 1994. Numerical simulation of faults and shear zones. Geophys. J. Int. 116, 46–52.
Fjaer, E., Holt, R.M., Horsrud, P., Raaen, A.M., Risnes, R., 2008. Petroleum Related Rock Mechanics, second ed. Elsevier.
Fortin, J., Millet, O., de Saxcé, G., 2003. Contruction of an averaged stress tensor for a granular medium. Eur. J. Mech. A Solids 22 (•), 567–582. http://dx.doi.org/10.1016/S0997-7538(03)00054-8.
Fossen, H., 2010. Structural Geology. Cambridge University Press.
Frye, K.M., Marone, C., 2002. The effect of particle dimensionality on granular friction in laboratory shear zones. Geophys. Res. Lett. 29 (19), 1916–1919. http://dx.doi.org/10.1029/2002gl015709.
Goscombe, B., Passchier, C., 2003. Asymmetric boudins as shear sense indicators - an assessment from field data. J. Struct. Geol. 25 (4), 575–589.
Goscombe, B.D., Passchier, C.W., Hand, M., 2004. Boudinage classification: end-member boudin types and modified boudin structures. J. Struct. Geol. 26 (4), 739–763.
Grasemann, B., Dabrowski, M., Schöpfer, M.P., 2019. Sense and non-sense of shear reloaded. J. Struct. Geol. 125, 20–28. http://dx.doi.org/10.1016/j.jsg.2018.05.028.
Grobe, A., Virgo, S., von Hagke, C., Urai, J.L., Littke, R., 2018. Multiphase structural evolution of a continental margin during obduction orogeny: Insights from the Jebel Akhdar Dome, Oman mountains. Tectonics 37 (3), 888–913. http://dx.doi.org/10.1002/2016TC004442.
Gueguen, E., Doglioni, C., Fernandez, M., 1997. Lithospheric boudinage in the western mediterranean back-arc basin. Terra Nova 9, 184–197. http://dx.doi.org/10.1046/j.1365-3121.1997.d01-28.x.
Hazzard, J.F., Mair, K., 2003. The importance of the third dimension in granular shear. Geophys. Res. Lett. 30 (13), http://dx.doi.org/10.1029/2003GL017534.
Hubbard, M.K., 1937. Theory of scale models as applied to the study of geologic structures. Geol. Soc. Am. Bull. 48 (10), 1459–1520. http://dx.doi.org/10.1130/gsab-48-1459.
Iyer, K., Podladchikov, Y.Y., 2009. Transformation-induced jointing as a gouge for interfacial slip and rock strength. Earth Planet. Sci. Lett. 280, 159–166.
Jaeger, J.C., Cook, N.G.W., Zimmermann, R.W., 2007. Fundamentals of Rock Mechanics, fourth ed. Blackwell Publishing.
Jolivet, L., Famin, V., Mehl, C., Parra, T., Aubourg, C., Hébert, R., Philippot, P., Whitney, D., Teyssier, C., Siddoway, C., 2004. Strain localization during crustal-scale boudinage to form extensional metamorphic domes in the aegean sea. In: Special papers-Geological Society of America. Boulder, Colo.; Geological Society of America; 1999, pp. 185–210.
Lamont, T.N., Smye, A.J., Roberts, N.M., Searle, M.P., Waters, D.J., White, R.W., 2023. Constraints on the thermal evolution of metamorphic core complexes from the timing of high-pressure metamorphism on Naxos, Greece. Bulletin 135 (11–12), 2767–2796.
Li, Y., Yang, C., 2007. On fracture saturation in layered rocks. Int. J. Rock Mech. Min. Sci. 44, 936–941.
Lloyd, G.E., Ferguson, C.C., 1981. Boudinage structure: some new interpretations based on elastic-plastic finite element simulations. J. Struct. Geol. 3 (2), 117–128. http://dx.doi.org/10.1016/0191-8141(81)90009-2.
Lohest, M., 1909. De l'origine des veines et des géodes des terrains primaires de belgique. Soc. Géol. Belg. Ann. 368, 275–282.
Maeder, X., Passchier, C.W., Koehn, D., 2009. Modelling of segment structures: Boudins, bone-boudins, mullions and related single- and multiphase deformation features. J. Struct. Geol. 31 (8), 817–830.
Mandal, N., Chakraborty, C., Samanta, S.K., 2000. Boudinage in multi-layered rocks under layer-normal compression - a theoretical analysis. J. Struct. Geol. 22, 373–382.
Mandal, N., Khan, D., 1991. Rotation, offset and separation of oblique-fracture (rhombic) boudins - theory and experiements under layer-normal compression. J. Struct. Geol. 13 (3), 349–356.
Mandl, G., 2005. Rock Joints The Mechanical Genesis. Springer.
Marques, F.O., Fonseca, P.D., Lechmann, S., Burg, J.P., Marques, A.S., Andrade, A.J., Alves, C., 2012. Boudinage in nature and experiment. Tectonophysics 526–529, 88–96. http://dx.doi.org/10.1016/j.tecto.2011.08.017.
Middleton, G.V., Wilcock, P.R., 1994. Mechanics in the Earth and Environmental Sciences. Cambridge University Press.
Mora, P., Place, D., 1994. Simulation of the frictional stick-slip instability. Pure Appl. Geophys. 143, 61–87.
Morley, C.K., von Hagke, C., Hansberry, R.L., Collins, A.S., Kanitpanyacharoen, W., King, R., 2017. Review of major shale-dominated detachment and thrust characteristics in the diagenetic zone: Part I, meso- and macro-scopic scale. Earth-Sci. Rev. 173, 168–228. http://dx.doi.org/10.1016/j.earscirev.2017.07.019.
Morley, C.K., von Hagke, C., Hansberry, R.L., Collins, A.S., Kanitpanyacharoen, W., King, R., 2018. Review of major shale-dominated detachment and thrust characteristics in the diagenetic zone: Part II, rock mechanics and microscopic scale. Earth-Sci. Rev. 176, 19–50. http://dx.doi.org/10.1016/j.earscirev.2017.09.015.
Mühlhaus, H.B., Vardoulakis, I., 1987. The thickness of shear bands in granular materials. Géotechnique 37 (3), 271–283.
Passchier, C.W., Druguet, E., 2002. Numerical modelling of asymmetric boudinage. J. Struct. Geol. 24, 1789–1803.
Passchier, C.W., Trouw, R.A.J., 1996. Microtectonics. Springer.
Paterson, M.S., Wong, T., 2005. Experimental Rock Deformation - The Brittle Field. Springer Berlin, Heidelberg, http://dx.doi.org/10.1007/b137431.
Peters, M., Veveakis, M., Poulet, T., Karrech, A., Herwegh, M., Regenauer-Lieb, K., 2015. Boudinage as a material instability of elasto-visco-plastic rocks. J. Struct. Geol. 78, 86–102. http://dx.doi.org/10.1016/j.jsg.2015.06.005.
Pincus, H., 2000. Closed-form / least-squares failure envelopes for rock strength. Int. J. Rock Mech. Min. Sci. 37, 763–785.
Place, D., Mora, P., 1999. The lattice solid model: incorporation of intrinsic friction. J. Int. Comp. Phys. 150, 332–372.
Place, D., Mora, P., 2001. A random lattice solid model for simulation of fault zone dynamics and fracture process. In: Mühlhaus H-B., D.A., Pasternak, E. (Eds.), Bifurcation and Localisation Theory for Soils and Rocks 99. AA Balkema Rotterdam/Brookfield.
Potyondy, D., Cundall, P., 2004. A bonded-particle model for rock. Int. J. Rock Mech. Min. Sci. 41 (8), 1329–1364.
Quirke, T.T., 1923. Boudinage, an unusual structural phenomenon. Bull. Geol. Soc. Am. 34 (4), 649–660.
Ramberg, H., 1955. Natural and experimental boudinage and pinch-and-swell structures. J. Geol. 63, 512–526.
Ramsay, J.G., Huber, M.I., 1987. The Techniques of Modern Structural Geology. Academic Press, London.
Reuning, L., Schoenherr, J., Heimann, A., Urai, J., Littke, R., Kukla, P., Rawahi, Z., 2009. Constraints on the diagenesis, stratigraphy and internal dynamics of the surface-piercing salt domes in the Ghaba Salt Basin (Oman): A comparison to the Ara formation in the South Oman Salt Basin. GeoArabia 32 (4), 83–120.
Roscoe, K.H., 1970. The influence of strains in soil mechanics. Géotechnique 20 (2), 129–170.
Schenk, O., Urai, J.L., van der Zee, W., 2007. Evolution of boudins under progressively decreasing pore pressure - a case study of pegmatites enclosed in marble deforning at high grade metamorphic conditions, Naxos, Greece. Am. J. Sci. 307, 1009–1033. http://dx.doi.org/10.2475/07.2007.03.
Schönherr, J., Reuning, L., Kukla, P., Littke, R., Urai, J., Rawahi, Z., 2008. Halite cementation and carbonate diagenesis of intra-salt carbonate reservoirs of the Late Neoproterozoic to Early Cambrian Ara Group (South Oman Salt Basin). Sedimentology 56 (2), 567–589.
Schöpfer, M.P.J., Abe, S., Childs, C., Walsh, J.J., 2009. The impact of porosity and crack density on the elasticity, strength and friction of cohesive granular materials: Insights from DEM modelling. Int. J. Rock Mech. Min. Sci. 46 (2), 250–261.
Schöpfer, M.P.J., Arslan, A., Walsh, J.J., Childs, C., 2011. Reconciliation of contrasting theories for fracture spacing in layered rocks. J. Struct. Geol. 33 (551–565), http://dx.doi.org/10.1016/j.jsg.2011.01.008.
Schöpfer, M.P.J., Childs, C., Walsh, J.J., 2007. Two-dimensional distinct element modeling of the structure and growth of normal faults in multilayer sequences: 1. Model calibration, boundary conditions, and selected results. J. Geophys. Res. 112, B10401. http://dx.doi.org/10.1029/2006JB004902.
van Gent, H., Urai, J.L., de Keijzer, M., 2011. The internal geometry of salt structures - A first look using 3D seismic data from the Zechstein of the Netherlands. J. Struct. Geol. 33, 292–311.
van Noten, K., Sintubin, M., 2010. Linear to non-linear relationship between vein spacing and layer thickness in centimetre- to decimetre-scale siliciclastic multilayers from the High-Ardenne slate belt (Belgium, Germany). J. Struct. Geol. 32 (3), 377–391. http://dx.doi.org/10.1016/j.jsg.2010.01.011.
Virgo, S., von Hagke, C., Urai, J.L., 2018. Multiphase boudinage: a case study of amphibolites in marble in the Naxos migmatite core. Solid Earth 9 (1), 91–113. http://dx.doi.org/10.5194/se-9-91-2018, URL https://se.copernicus.org/articles/9/91/2018/.
von Hagke, C., Bamberg, B., Virgo, S., Urai, J.L., 2018. Outcrop-Scale Tomography: Insights into the 3D Structure of Multiphase Boudins. California Digital Library (CDL), http://dx.doi.org/10.31223/osf.io/4kt9x.
Wang, Y., Abe, S., Latham, S., Mora, P., 2006. Implementation of particle-scale rotation in the 3-D lattice solid model. Pure Appl. Geophys. 163, 1769–1785.
Weatherley, D., 2011. Investigations on the role of microstructure in brittle failure using discrete element simulations. Geophys. Res. Abstr. 13, EGU2011–9476.
Weatherley, D., Boros, V., Hancock, W., Abe, S., 2010. Scaling benchmark of esys-particle for elastic wave propagation simulations. In: Sixth IEEE International Conference on EScience. Brisbane, Australia.

Zulauf, G., Zulauf, J., Bornemann, O., Brenker, F., Höfer, H., Peinl, M., Woodland, A., 2010. Experimental deformation of a single-layer anhydrite in halite matrix under bulk constriction. Part 2: Deformation mechanisms and the role of fluids. J. Struct. Geol. 32 (3), 264–277. http://dx.doi.org/10.1016/j.jsg.2009.12.001.

Zulauf, G., Zulauf, J., Bornemann, O., Kihm, N., Peinl, M., Zanella, F., 2009. Experimental deformation of a single-layer anhydrite in halite matrix under bulk constriction. Part 1: Geometric and kinematic aspects. J. Struct. Geol. 31, 460–474. http://dx.doi.org/10.1016/j.jsg.2009.01.013.